Regular Article - Flowing Matter

Particle shape effect on the structural evolution and force propagation inside the three-dimensional sandpile

Qiong Xiao[a]

School of Civil Engineering, Southeast University, Nanjing 210096, Jiangsu, China

Abstract This paper employs the discrete element method to examine the impact of particle shape on the pressure dip phenomenon and structural characterization of the three-dimensional sandpiles. Particular attention has been given to the underlying mechanism in the sandpile, which arises from the interplay of the initial created structure and the induced changes in the subsequent deposition process. Different aspect ratios produced different initial local geometry. The contact vector and strong contact force rotated away from the z-axis when the aspect ratio deviates from 1.0. The flat particles had a better memory of initial structures under the subsequent deposition process, which plays a vital role in force transmission and stress propagation. However, when the aspect ratio approaches 1.0, the stress state behaves as a joint result of maintained and gained contacts. For a certain range of aspect ratios, the newly generated interactions of elongated particles induced the major stress in the horizontal plane, which thus produces a significant pressure dip phenomenon. The results indicated that complex models accounting for contact creation are required to capture the pressure profile.

1 Introduction

Richard et al. [1] proposed that granular materials are the second-most manipulated material in nature after water, which is mainly non-spherical with complex shapes like sands, pharmaceutical tablets, food grains, biomass particles, etc. Hence, a comprehensive understanding of the effect of particle shape on the behaviour of granular packing is important for the design, optimization and scale-up of industrial applications [2]. Sandpile is one of the simplest structures of granular packing, which exhibits many phenomena such as segregation [3] and stratification [4] that are not yet fully understood. Our study is focused on the pressure dip phenomenon. It refers to a depression in the normal pressure underneath the apex of the sandpile. To the author's knowledge, Hummel and Finnan [5] were the first experimentally observed the pressure dip phenomenon underneath a sandpile using the point deposition method, which has attracted extensive investigations since the 1980s. Over the last couple of decades, several influential factors and mechanisms have been extensively investigated, including but not limited to particle morphology [6–13], deposition process [14–16] and base plane deflection [17,18].

Among the factors, particle shape is an important aspect in controlling the fabric of granular materials. Fitzgerald et al. [19] proposed that the flow behaviour

of non-spherical particles is quite different from that of perfect spheres, which can result in different packing patterns, ability to fluidize and angle of repose. Matuttis et al. [20] and Zhou and Ooi [21] found that the angle of repose is enhanced with the increase of the non-sphericity. Change in the angle of repose would influence the arrangement of particles and the stress propagation. Zuriguel and Mullin [8,9] reported that the non-spherical particles such as ellipsoid and pear shape could generate a larger repose angle with a more unambiguous pressure dip phenomenon.

The macroscale behaviour of granular materials depends on the collective outcome of individual particles. With the development of numerical techniques, simulations can investigate microscopic parameters that are not accessible to experiments. The discrete element method (DEM) is a powerful tool to provide particle-scale information on granular materials without any arbitrary assumptions. Some works can be found in the literature to examine the particle shape effects on the pressure dip phenomenon. Ai et al. [22] studied the stress distribution with the clumped particles. Similar to the experimental work, they found that the concentrated deposition produces an inclined contact orientation, which is proposed to result in the pressure dip phenomenon. Zhu et al [23] considered the impact of the particle aspect ratio on the behaviour of the pressure dip phenomenon. Results presented that the degree of pressure dip phenomenon increased with a higher aspect ratio, with particles oriented in the hor-

[a] e-mail: xiaoqiong@seu.edu.cn (corresponding author)

izontal direction. Liu et al. [24] constructed the conical sandpiles with ellipsoids particles and demonstrated that the force structures vary significantly with the aspect ratios of ellipsoids.

As reported in the literature, the particle shape would influence the connectivity and force networks of the sandpile. Previous works are mainly limited to the two-dimensional sandpile to explore the properties. Compared with the two-dimensional system, the lateral forces constraining the three-dimensional sandpile are more complex [25]. Hence, more work is needed to improve understanding of the pressure dip phenomenon and the underlying mechanisms of three-dimensional sandpiles. Our study is focused on the particle shape effects on the heterogeneity and forces propagation using the three-dimensional DEM simulation. This paper is structured as follows, Sect. 2 introduces the methodology for contact detection and the implementation of the numerical model. We present the macroscale behaviour of sandpiles in Sect. 3. The structural properties and contact force are displayed in Sects. 4 and 5, respectively. Section 6 discusses the pressure dip phenomenon by the underlying mechanisms of initial structure and the induced heterogeneous geometry. Finally, we conclude and draw the future outlook of this work.

2 Methodology

Various methods have been proposed in the literature to generate the complex shapes of particles, such as the ellipsoid particle [26], polar form of particles [27,28], polygon particles [29] and multi-spheres particles [30]. The literature implies that the dip requires a large enough pile compared to the grain size. Hence, the computational efficiency in contact detection plays a vital role in the DEM simulation. Concerning the clumped particles, Soltanbeigi et al. [31] proposed that this method requires enough spherical particles to construct a smooth surface, and the rough surface may increase the coordination number of particles. An alternative approach is using the superquadric shape to define the non-spherical particle, with the calculation method first proposed by Barr [32]. Wiliams and Pentland [33] first applied this algorithm in the two-dimensional DEM simulation and suggested that 80% of all shapes can be represented by the superquadric function. Thus, this method is employed in this study to investigate the shape effect on the mechanisms of sandpile using the LIGGGHTS (LAMMPS Improved General Granular and Granular-heat Transfer Simulations) software. The following sections give a detailed introduction of the algorithm, a comparison of the shape effect on the simulation time and the implementation of the numerical model.

2.1 Particle definition

LIGGGHTS defines the shape of superquadric particle using the following expression,

$$f(x,y,z) = \left(|\frac{x}{a}|^{n_2} + |\frac{y}{b}|^{n_2} \right)^{\frac{n_1}{n_2}} + |\frac{z}{c}|^{n_1} - 1 = 0 \quad (1)$$

where a, b, c denote the half-length of the particles along its principal axes. n_1, n_2 are the blockiness parameters to control edge sharpness. Change the five parameters can vary the size and shape of particles from rounded to nearly cubical simplicity. The ellipsoid particles are modelled with $n_1 = n_2 = 2$ and $a \neq b \neq c$. The cylinder particle shape is composed by $n_1 = 2, n_2 \geq 2$, and if $n_1 \geq 2, n_2 \geq 2$, the particle is in a box-like shape.

2.2 Contact detection

Compared with the spherical particles, the interaction of non-spherical particles is more complex. Hence, it is essential to optimize the algorithm of contact detection for improving computational efficiency. Ericson [34] proposed that the computational time can be reduced using bounding volumes in contact detection pre-steps. The LIGGGHTS software employs this strategy to narrow contact detection. It is first approximated by the bounding spheres, with the size determined as $R = \sqrt{(a^2 + b^2 + c^2)}$. If the distance between the centres of spheres is less than the sum of the radii, the particles are intersected, otherwise are not in contact. The minimum oriented bounding boxes (OBB) is used for the second survey, determined as a rectangular block with semi-axes (a, b, c) and oriented axes, which checks the interaction between two OBBs based on the concept of the separation axis. For an arbitrary vector $\mathbf{u}$, the OBBs are regarded as interacted if the projections of these boxes on $\mathbf{u}$ are intersected.

Then, the contact point is determined based on a "midway" point $\mathbf{X}_0$ between two superquadric particles i and j. Applying Lagrange multipliers, this optimization problem becomes a solution of the following nonlinear system [35],

$$\begin{cases} \nabla F_i(\mathbf{X}) + \mu^2 \nabla F_j(\mathbf{X}) = 0 \\ F_i(\mathbf{X}) - F_j(\mathbf{X}) = 0 \end{cases} \quad (2)$$

where $\mathbf{X} = (x, y, z)^{\mathrm{T}}$. μ is the proportionality coefficient. F is the shape function of a superquadric particle in a global frame, which defines as $F_i = f(\mathbf{A}_i^{\mathrm{T}} \cdot (\mathbf{X} - \mathbf{X}_{ci})$ for particle i. $\mathbf{X}_{ci}$ is the centre of the superquadric particle i in the global frame. $\mathbf{A}_i = \mathbf{A}(\mathbf{q}_i)$ is the quaternion-based rotation matrix, determined by $\mathbf{q}_i = (q_0, q_1, q_2, q_3)^{\mathrm{T}}$ and expressed as

$$\mathbf{A}_i = \begin{bmatrix} q_0^2 + q_1^2 - q_2^2 - q_3^2 & 2(q_1 q_2 + q_0 q_3) & 2(q_1 q_3 - q_0 q_2) \\ 2(q_1 q_3 - q_0 q_3) & q_0^2 - q_1^2 + q_2^2 - q_3^2 & 2(q_2 q_3 + q_0 q_1) \\ 2(q_1 q_3 + q_0 q_2) & 2(q_2 q_3 - q_0 q_1) & q_0^2 - q_1^2 - q_2^2 + q_3^2 \end{bmatrix}.$$

$\nabla F_i(\mathbf{X})$ is 1st (gradient) derivatives of the shape function. If the "midway" point $\mathbf{X}_0$ satisfies conditions $F_i(\mathbf{X}_0) < 0$ and $F_j(\mathbf{X}_0) < 0$, the contact between two particles takes place with the contact point $\mathbf{X}_0$. The

nearest intersection points $\mathbf{X}_j$ and $\mathbf{X}_i$ between the contact line and surfaces of particles i and j are expressed as,

$$F_i(\mathbf{X}_i) = 0, \quad \text{where} \quad \mathbf{X_i} = \mathbf{X}_0 + \alpha_i \mathbf{n_{ij}},$$
$$F_j(\mathbf{X}_j) = 0, \quad \text{where} \quad \mathbf{X_j} = \mathbf{X}_0 + \alpha_j \mathbf{n_{ij}}. \quad (3)$$

where $\mathbf{n}_{ij}$ is the normal overlap direction, estimated as $\mathbf{n}_{ij} = \nabla F_i / \|\nabla F_i\|$ at the contact point $\mathbf{X}_0$. Then, the normal overlap vector is $\delta_n \equiv \mathbf{X}_i - \mathbf{X}_j = (\alpha_i - \alpha_j)\mathbf{n}_{ij}$. The scalars α_i and α_j can be easily obtained by Newton's iterations,

$$\alpha_i^{k+1} = \alpha_i^k - \frac{f(\mathbf{X}_i^k)}{\nabla f(\mathbf{X}_i^k) \cdot \mathbf{n}},$$
$$\alpha_j^{k+1} = \alpha_j^k - \frac{f(\mathbf{X}_j^k)}{\nabla f(\mathbf{X}_j^k) \cdot \mathbf{n}}. \quad (4)$$

2.3 Contact force

The interparticle force includes the normal force and tangential force, which both contain a spring force and a damping force. This study conducts the simulations using the Hertz contact model. A nonlinear damping term proposed by [36] has been used in the simulations. The damping coefficient is an empirical constant related to the restitution coefficient (e) as a function of the incoming velocity in elastoplastic collisions. Equation 5 gives the expression of the normal and tangential force.

$$\mathbf{F}_n = k_n \delta_n - \gamma_n \mathbf{v}_n,$$
$$\mathbf{F}_t = \min(k_t \delta_t - \gamma_t \mathbf{v}_t, \mu_s |F_n|). \quad (5)$$

where $\mathbf{F}_n$ and $\mathbf{F}_t$ are the normal force component and tangential force component, respectively. μ_s is the coefficient of sliding friction. $\mathbf{v}_n$ and $\mathbf{v}_t$ denote the normal component and tangential component of the relative velocity, respectively. The normal relative velocity between particle i and j estimates as $\mathbf{v}_n = ((\mathbf{v}_j - \mathbf{v}_i) \cdot \mathbf{n}_{ij})$, and the tangential relative velocity equals $\mathbf{v}_t = \mathbf{v}_j - \mathbf{v}_i - \mathbf{v}_n$, where $\mathbf{n}_{ij}$ is the normal overlap direction. δ_t is the tangential overlap, which represents the elastic tangential deformation of the particle surfaces that happened since particles touched at t_0 and estimates as $\delta_t = \int_{t_0}^t \mathbf{v}_t \, dt$.

k_n, k_t are the normal and tangential spring coefficients, and γ_n, γ_t are the normal and tangential damping coefficients, respectively, expressed as,

$$k_n = 4E^* \sqrt{R^* \delta_n}/3, \quad k_t = 8G^* \sqrt{R^* \delta_n},$$
$$\gamma_n = -2\sqrt{\tfrac{5}{6}}\beta\sqrt{S_n m^*}, \quad \gamma_t = -2\sqrt{\tfrac{5}{6}}\beta\sqrt{S_t m^*}. \quad (6)$$

where $S_n = 2E^*\sqrt{R^*\delta_n}$, $S_t = 8G^*\sqrt{R^*\delta_n}$. β is a coefficient of restitution, estimated as $\beta = \frac{\ln(e)}{\sqrt{\ln^2(e)+\pi^2}}$. G^*, E^* and R^* are the equivalent shear modulus, Young's modulus and radius, respectively. $R^* = \frac{R_i R_j}{R_i + R_j}$, which is critical for the calculation of k_n, k_t, γ_n and γ_t. We use local curvature radius at the contact point as

Table 1 Key parameters used in the DEM simulations

Density	2700 kg/m^3
Equivalent diameter of a sphere	1.2 mm
Young's modulus	70 GPa
Friction coefficient	1.0
Restitution coefficient	0.5
Poisson ratio	0.35
Time-step (s)	6.27×10^{-7}

particle radius, estimated as $R = 1/K$, where $K = K_{\text{mean}} = \frac{(\nabla F^{\mathrm{T}} \cdot \nabla^2 F \cdot \nabla F - |\nabla F|^2 (F_{xx} + F_{yy} + F_{zz}))}{2|\nabla F|^3}$, $\nabla^2 F$ is the 2nd (Hessian matrix) derivatives of the shape function. A detailed introduction for contact detection and contact force calculation can be found in [35].

In a granular system, a given particle involves translational and rotational motion. In DEM, each particle i is tracked by explicitly solving their trajectories using Eq. 7, which are governed by Newton's second law of motion,

$$m_i \ddot{\mathbf{X}}_i = \mathbf{F}_i,$$
$$\dot{\mathbf{L}}_i = \mathbf{T}_i \quad (7)$$

where m_i and $\mathbf{X}_i$ are the mass and position of the particle centre. $\mathbf{F}_i$ and $\mathbf{T}_i$ are the total force and total torque acting on the particle, respectively. $\mathbf{L}_i = \mathbf{I}_i \cdot \omega_i$ is the angular momentum of the particle i. $\mathbf{I}_i$ is the tensor of inertia and ω_i is the angular velocity in the global frame.

Accurate determination of a particle's orientation is critical for determining the angular velocity of a superquadric particle [35]. We employ the particle-based coordinate system to model the rotation of the superquadric particles, which yields the following expression,

$$\hat{\mathbf{I}}_i^L \dot{\omega}_i^L + \omega_i^L \times \hat{\mathbf{I}}_i^L \omega_i^L = \mathbf{T}_i^L \quad (8)$$

where $\hat{\mathbf{I}}_i^L$ is the principal tensor of inertia. ω_i^L and $\mathbf{T}_i^L$ are the angular velocity and angular moment in the particle-based coordinate system, respectively. Based on the rotation matrix A, the torque and angular velocity in the global frame can be easily obtained as $\mathbf{T}_i^L = \mathbf{A} \cdot \mathbf{T}_i$, $\omega_i = \mathbf{A}^{\mathrm{T}} \cdot \omega_i^L$, where $\mathbf{A}^{-1} = \mathbf{A}^{\mathrm{T}}$.

The LIGGGHTS software uses the velocity Verlet integration scheme to calculate position and velocity as a function of time [37], which contains two steps. The first step is to update the velocities by a half-time-step and positions by one step, and then compute the interaction forces between the particles and their neighbours to update the velocities by another half-step.

2.4 Material properties

Cleary and SawLey [38] found that the average mass flow rate predicted for discharge from the hopper was reduced when increases the blockiness. The simulation

requires enough large-scale systems to observe the pressure dip phenomenon. Hence, we select the ellipsoids for the simulations to reduce the computational time. The equivalent diameter of a sphere is set to 1.2 mm based on the experimental work of Vanel et al. [39]. Young's modulus is 70 GPa, which is the typical value of silica. The value of the restitution coefficient is chosen based on the single-degree-of-freedom system [36] as 0.5. The particle friction is 1.0 in order to achieve a relatively steeper conical sand pile for the spheres. We have not considered the rolling resistance of particles in this study to involve no unnecessary complexity. The LIGGGHTS software determines the critical time-step by the time through a particle with the Rayleigh wave proposed by Johnson [40], expressed as,

$$t = \pi r \times \sqrt{\frac{\rho}{G}}/(0.1631\nu + 0.8766) \qquad (9)$$

where ρ and r are the density and radius of particles respectively. G is the shear modulus and ν is the Poisson's ratio. This study adopts the equivalent radius of a sphere to estimate the time-step, which is 6.27×10^{-7} s. Table 1 lists the key simulation parameters.

2.5 Validation of the numerical models

2.5.1 Numerical model set-up

It is generally known that the pressure dip phenomenon is dependent on construction history. Two pile formation processes, the point deposition and rain deposition methods, have been simulated to validate the numerical models. Figure 1 illustrates the configuration of the numerical model. The hopper and the sieve are used in the point deposition and rain deposition methods, respectively, located at 60 mm above the base plane. The diameter of the hopper outlet equals 12 mm, which is ten times the particle diameter. The sieve diameter is set at 140 mm, the same size as the base plane. We define particles by the aspect ratio (α), determined as $\alpha = a/c$, and $b = c$, which equals 0.5. During the simulation process, particles are continuously generated inside the hopper/sieve and deposited to the base plane under the acceleration of 9.81 m/s^2. Moreover, particles running off below the base plane would be deleted to save computational effort. The graph suggests that point deposition forms the sandpile by geometry, while rain deposition constructs the heap layer by layer.
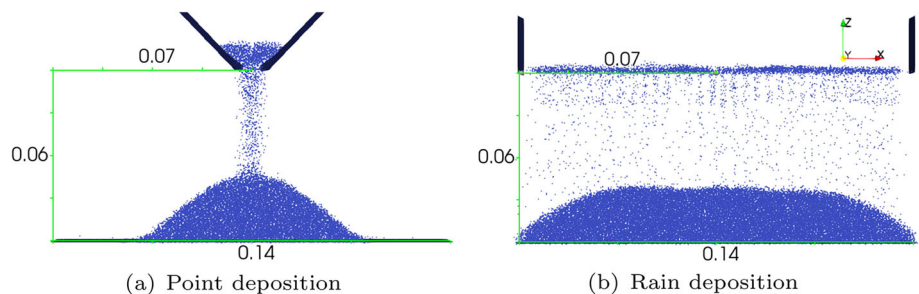
DEM simulations cannot achieve the complete static condition, particularly for the free surface region of the sandpile. The material is in an equilibrium state when the forces acting on the particles are self-balanced. Hence, the unbalanced force, as the total force acting on the particles, is an index to identify the equilibrium condition. We regard the system in an equilibrium condition if the ratio of the average unbalance force to average contact force is below an acceptable tolerance ($\delta_{\rm tol}$), expressed as,

$$\frac{f_{\rm ub}}{f_{\rm ac}} \le \delta_{\rm tol} \qquad (10)$$

where $f_{\rm ub}$ and $f_{\rm ac}$ denote the average unbalance force and average contact force, respectively.

Li et al. [41] proposed that most kinetic energy of a given boundary work was dissipated when the unbalanced force ratio is less than 0.01. We thus adopt the tolerance as 0.01 in this study. Figure 2 depicts the spatial distribution of the particle velocity in the ($r - z$) space to verify the static state of the sandpile. The graph shows the structure is in a quasi-static condition after the sandpile is constructed, particularly for the central heap. This study aims to understand the initial heap formation and growth on the behaviour of the pressure dip phenomenon and structural characterization in the inner region. Hence, to certify the static condition, we further checked the ratio of the kinetic energy to the potential energy for the central heap, which is less than 0.008 and identified a quasi-static regime.

2.5.2 Base plane pressure profile

One of the main interests of the sandpile problem is the pressure dip phenomena, which is relevant to the stresses that sandpiles impose on the base plane. Hence, we are only concerned about the interaction with the base plane to interpret the base pressure. Due to the axis-symmetric conical sandpile, the stress state is analysed in the cylindrical coordinate system.

For each particle, at the coordinate (x, y, z), the contact force (f_x, f_y, f_z) in the Cartesian coordinate system is converted into components (f_r, f_ϑ, f_z) in the cylindrical coordinate system using Eq. 11,

$$\begin{cases} f_r = f_x \cos\theta + f_y \sin\theta \\ f_\vartheta = -f_x \sin\theta + f_y \cos\theta \\ f_z = f_z \end{cases} \qquad (11)$$
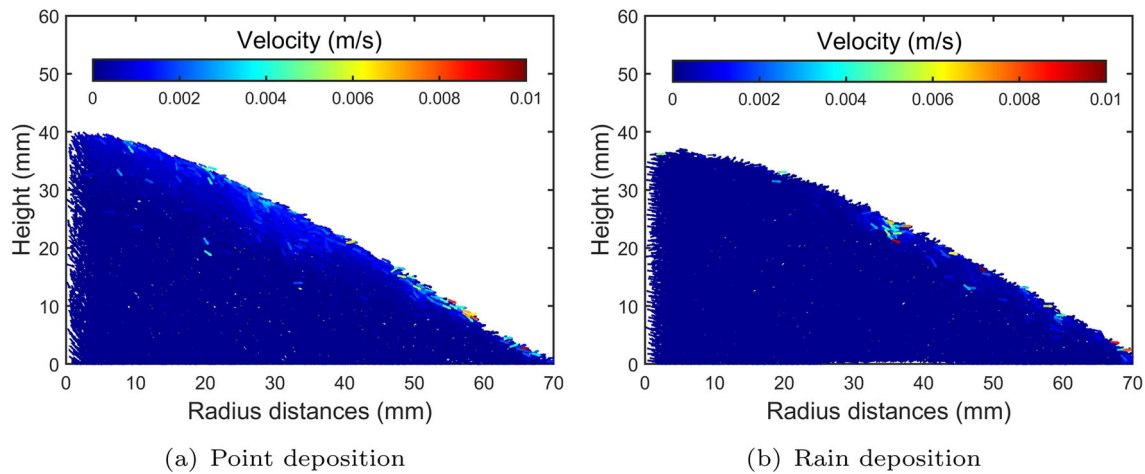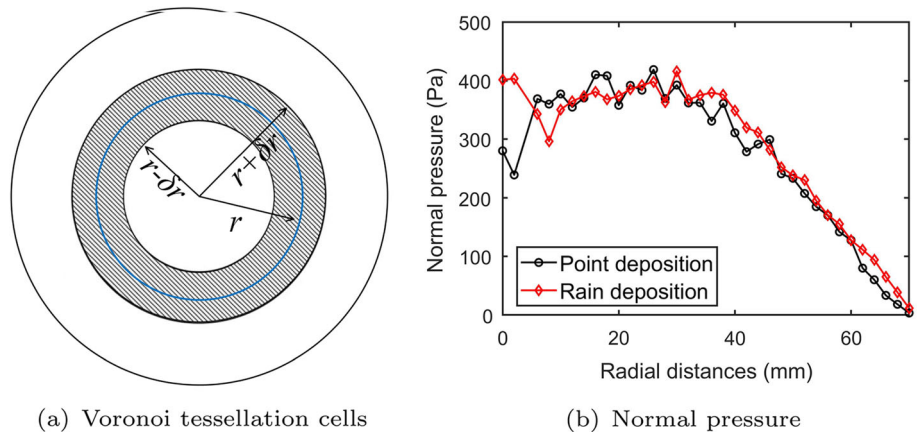
Fig. 1 The configuration of the numerical models (unit: m)

(a) Point deposition

(b) Rain deposition

(a) Point deposition

(b) Rain deposition

Fig. 2 Spatial distribution of particle velocity

Fig. 3 Base plane pressure distribution under different construction histories

(a) Voronoi tessellation cells

(b) Normal pressure

where $\theta = \arctan(y/x)$.

Previously reported experiments used pressure cells to record the forces acting within the cell area to estimate pressure distributions [5,16]. Following a similar spirit, we use the annulus-based average method to estimate the stress, measured by summing up all the components of contact forces falling within the concentric rings over the corresponding annulus area. At radius r, as shown in Fig. 3a, the annulus area (A_r) refers to the region within $(r - \delta r/2)$ and $(r + \delta r/2)$, estimated as $A_r = \pi((r + \delta r/2)^2 - (r - \delta r/2)^2)$, where δr equals 2 mm. The stress components are then measured as $\tau_r = f_r/A_r$, $\tau_\theta = f_\vartheta/A_r$, $\sigma_n = f_z/A_r$, where σ_n, τ_r and τ_θ refer to the normal, radial shear and circumferential shear stress, respectively. In this section, we study the pressure dip phenomenon from the estimation of normal pressure on the base plane, as shown in Fig. 3b. The graph shows the pressure dip phenomenon only occurs under the point deposition method, which agrees well with the previous laboratory observations [39,42] and validates the numerical models. We thus adopt the point deposition test to observe the particle shape on the influence of the pressure dip phenomenon.

3 Simulation results

We predominantly define different particle shapes by varying the aspect ratio (α). Particles are oblate when $\alpha < 1$, which becomes prolate when $\alpha > 1$. Seven different aspect ratios are selected, as 0.25, 0.5, 2/3, 1, 1.5, 2 and 3, to produce shapes from oblate to prolate. Particles are continuously inserted into the hopper and deposited to the base plane for the formation of the sandpile, following the process described in Sect. 2.5. This section describes the macroscale properties of sandpiles and examines the base pressure profile with different particle shapes.

3.1 Sandpile properties

Packing density is a common feature for determining the structural characteristics of the packing problem, which involves numerous works focusing on the correlation between packing fraction and sphericity [43,44]. Here, we measure the total volume of the sandpile (V) by the convex hull volume of discrete points and estimate the average packing fraction as $n = V_s/V$, where V_s is the solid volume of particles. Figure 4 depicts the relationship between packing fraction and aspect ratio.
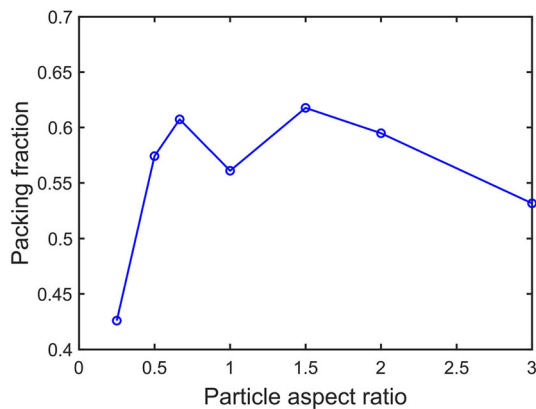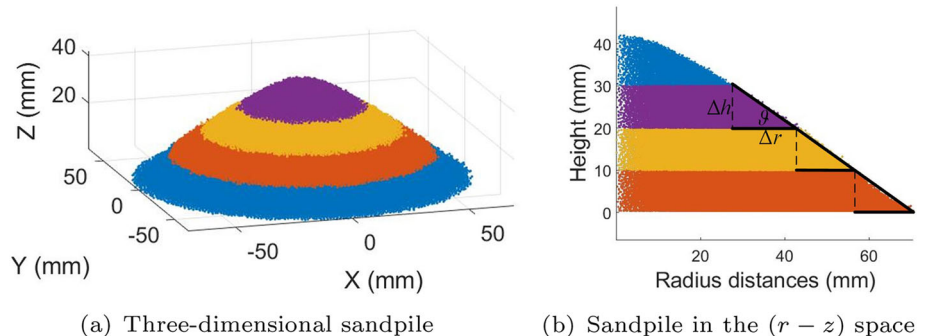
Fig. 4 The evolution of packing fraction with particle aspect ratio

Similar to the packing problem reported in [44], the sandpile problem also gives an M-shaped curve for the relationship between packing fraction and sphericity. The graph displays that ellipsoidal particles can achieve a denser sandpile than spherical particles within a specific range of aspect ratios. However, the packing density would become looser than spheres when the particles are too flat or elongated, particularly for the oblate particles.

The repose angle is an essential parameter for understanding the micro-behaviour of the granular material and relating to the macro-behaviour [45]. The commonly used definition of the repose angle is the steepest slope of the materials heaped without collapsing [46]. Generally, the surface contours are not strictly planar, particularly for the top surface. We thus subdivide the heap into multiple layers to illustrate the sandpile profile, depending on the z-coordinate of particles, as shown in Fig. 5a. The dimension of each layer is 10 mm in the z-direction. Figure 5b displays the graph in

the $(r - z)$ space to measure the repose angle by the inverse tangent (arctan) rule for each layer and estimate as $\vartheta = \arctan(\Delta h/\Delta r)$, where Δh and Δr refer to the relative height and relative radius distance for the envelope of the sandpile, respectively. Table 2 presents the results. As expected, spherical particles achieve the lowest repose angle, which increases when the particle becomes more irregular. Moreover, the oblate particles produce a steeper sandpile than the prolate particles.

3.2 Stress distribution on the base plane

Following the procedures described in Sect. 2.5, the base plane pressure profile with different aspect ratios can be obtained, as shown in Fig. 6. Due to the lower height, the sandpile with $\alpha = 1$ produces a relatively lower normal pressure and radial shear stress. As expected, the circumferential shear stress τ_θ is close to zero concerning the axis-symmetric system. The stress profiles fluctuate and produce local variations due to the inherent randomness impact for granulate systems. Hence, the difference in the pressure profile is not clear from the scattered data point, particularly for the normal pressure. The aspect ratio induces a significant difference in the behaviour of the radial shear stress, with a higher peak magnitude observed for $\alpha = 0.25$. For the normal pressure, the polynomial fitting curves are plotted for different aspect ratios to describe the pressure dip phenomenon. The relative pressure dip (d_p) is quantified by $(\sigma_n^p - \sigma_n^a)/\sigma_n^p$, where σ_n^p refers to the peak normal pressure and σ_n^a denotes the normal pressure underneath the apex of the sandpile. Table 3 presents the specific values of d_p for different aspect ratios, with the peak magnitude occurring at $\alpha = 2$. The results indicate that the pressure dip phenomena enhance with the shape changes from the spheres to ellipsoids. For the oblate and prolate particles, a relatively higher d_p is observed at $\alpha = 0.5$ and $\alpha = 2$, respectively.
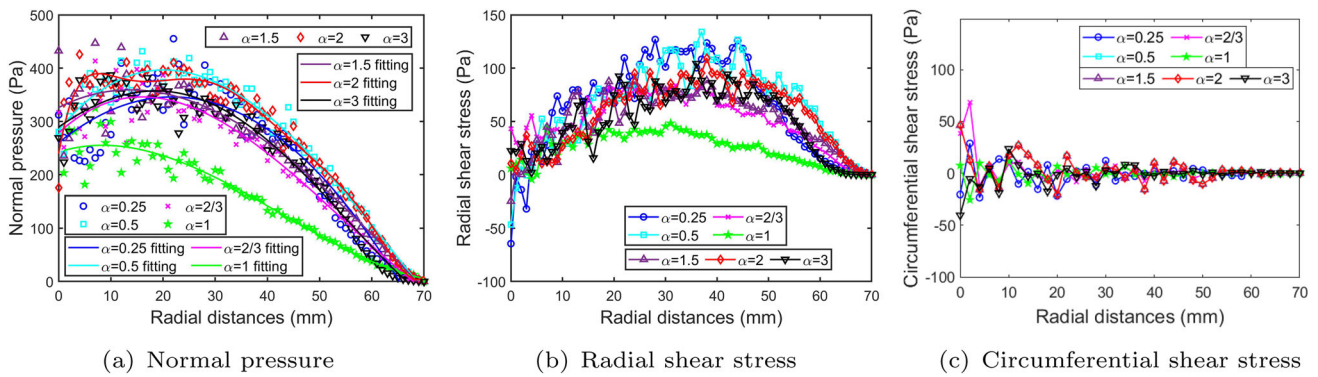
Fig. 5 A schematic figure of the measure of repose angle

(a) Three-dimensional sandpile

(b) Sandpile in the $(r - z)$ space

Table 2 Repose angle of sandpiles with different particle aspect ratios

Height	$\alpha = 0.25$	$\alpha = 0.5$	$\alpha = 2/3$	$\alpha = 1$	$\alpha = 1.5$	$\alpha = 2$	$\alpha = 3$
(0~10) mm	24.73°	34.29°	28.55°	16.85°	28.87°	33.39°	28.7°
(10~20) mm	42.39°	34.08°	28.0°	21.44°	28.88°	35.15°	39.16°
(20~30) mm	45.94°	32.76°	28.41°	–	27.59°	30.38°	31.08°
Average	37.69°	33.71°	28.32°	19.15°	28.45°	32.97°	32.98°

(a) Normal pressure   (b) Radial shear stress   (c) Circumferential shear stress

Fig. 6 Base plane pressure distribution with different aspect ratios

Table 3 Pressure dip of sandpiles with different aspect ratios

Aspect ratio (α)	0.25	0.5	2/3	1	1.5	2	3
Relative pressure dip (%)	24.87	28.45	19.52	3.79	9.21	38.49	19.02

4 Spatial structural characteristics of sandpile

Stresses that sandpiles impose on the base plane are highly related to the forces transmitted inside the sandpile. Generally, the interparticle forces are related to the arrangement and connectivity of particles. Hence, it is essential to examine the structural properties of sandpiles for understanding the pressure profile constructed. One of the most compelling continuum models reported in the literature is the fixed principal axis (FPA) model proposed by Wittmer et al. [47,48], which raised sensational attention as the simple model successfully reproduced the pressure dip phenomenon. They assumed particles embedded frozen at the instant of deposition, which means particles have a good memory of the initial structure. We thus identify the structural properties of the sandpile problem by the initial and induced properties for elucidating the underlying mechanisms and whether the traditional continuum mechanics approach can explain the pressure dip phenomenon.

4.1 Initial state of sandpile

The subsequent loading process implies the sandpile generated by geometry under the point deposition method. Hence, the initial local geometry refers to a minimum available structure to form a specific pile, defined by around 17,000 particles deposited in this study. Al-Hashemi and Al-Amoudi [45] proposed that factors like density, anisotropy and particle arrangement will determine the material structure, while the particle shape, size, contacts and distribution will control the fabric. We thus examine the characteristics of void ratio, coordination number, contact orientation and particle orientation to understand this complex structure.

4.1.1 Void ratio

The Voronoi tessellation method is widely adopted to determine the local void ratio, which subdivides the domain into small cells with each cell containing only one particle. The cell is constructed by the points with distances to the particle surface no greater than those to other particles. The originally Voronoi tessellation concerns the volumeless points, which may affect the formation of polyhedrons in the three-dimensional space and influence the characteristics of local structures, particularly for the non-spherical particles. Hence, it requires a rigorous technique to generate the Voronoi cells for analysing the spatial properties of the sandpile. The literature presents several methods to obtain the Voronoi cells of non-spherical particles, for instance, a Voronoi channel method based on tracking the imaginary empty sphere of variable size inside a packing [49] and a universal numerical method proposed in the X-ray tomography [50]. This study employs the three-dimensional Set Voronoi diagram method to form the Voronoi tessellation cells for the data analysis.

The Set Voronoi diagram is defined in analogy to the definition of the conventional Point Voronoi diagram, with the distances between a point $\mathbf{x}$ and a discrete particle K measured to the nearest point on the bounding surfaces of the particle, rather than to the particle centre. Hence, it consists of three steps to generate Voronoi cells: first, it creates a sufficiently dense set of points to represent the discretization of the bounding surfaces of the particles, and second, creates a lookup for particle indices and computes the conventional Point Voronoi diagram of these particles, and finally, identifies the set of Voronoi facets for each particle and merges the Point Voronoi cells via removing the Voronoi facets whose dual Delaunay edge connects two points belong to the same particle. A detailed introduction to the algorithm can be found in Schaller et al. [51].
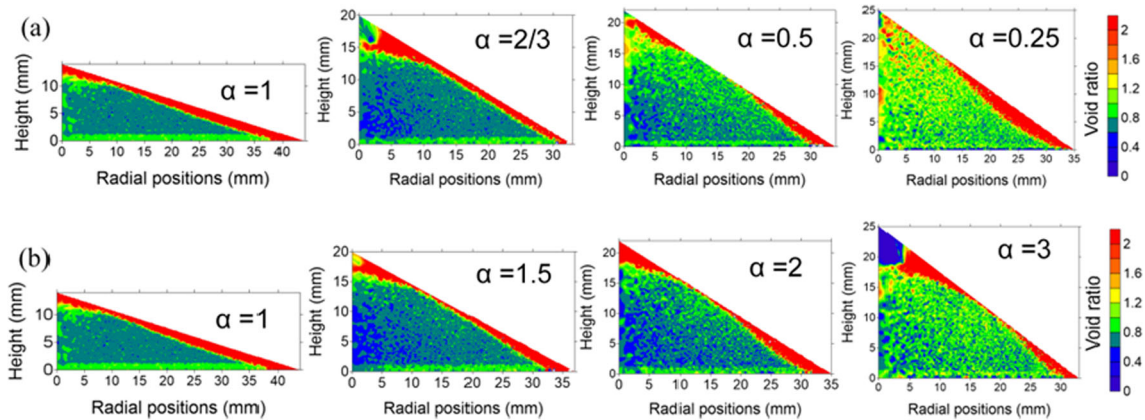
Fig. 7 Spatial distribution of void ratio: **a** oblate particles and **b** prolate particles

The volume of each particle is determined as the cell volume to estimate the local void ratio. Figure 7 portrays the spatial distribution of the void ratio in the $(r - z)$ space. At position (r, z), the void ratio refers to the circumferential average of particles located inside a hollow cylindrical region, which is determined by two coaxial cylindrical surfaces of radii, $(r - \delta r/2)$ and $(r + \delta r/2)$, with the height in $(z - \delta z/2, z + \delta z/2)$, where δr and δz both equal 2 mm. The contour graph is plotted by the position of particles and coloured by the results of the void ratio. This study concerns the domain as a cubic container, which may generate larger Voronoi cells for particles at the edges of the sandpile. In such a case, the graphs display a significantly higher void ratio near the free surface for each sandpile. It requires addressing the irregular boundary conditions in future work. It has been that the formation process induces a long runout distance of spherical particles. Hence, under the same number of particles, the spheres construct the sandpile with a higher radius distance and lower height, resulting in a relatively loose packing than the oblate and prolate particles. The results indicate that particles in a specific range of aspect ratios generate a denser initial local geometry underneath the apex of the sandpile. However, when the particle becomes too flat or elongated, the void ratio increases inside the sandpile, especially for the flat particles.

4.1.2 Coordination number

Coordination number (CN), referred to as the density of contacts per particle within a granular assembly, is a classic measure to characterize the packing structure. In analogy to the void ratio, Fig. 8 depicts the spatial distribution of the coordination number. For the point deposition method, particles are rolled down from the apex to form the sandpile, generating the flow behaviour of particles near the free surface and showing the lowest coordination number. The graph shows a remarkably lower coordination number for the spherical particles than the non-spherical particles. Baule and Makse [52] proposed that the spherical packings can lead to an increase in the coordination number from 4

to 6 between the random loose packing (RLP) and random close packing (RCP). Figure 7 shows that the void ratio is in the span of $(0.6, 1.2)$ for the spheres; hence, the solid fraction ranges from 0.45 to 0.625. According to Makse et al. [53], the sandpile of spheres constructs a lower solid fraction than the RLP. The results agree with the work of Horabik et al. [54], implying that the pile of spherical particles with a high value of sliding friction is in a much looser state than the RLP and obtains a lower coordination number than the limiting value of 4. For different aspect ratios, we can observe that the coordination number enhances under the apex of the sandpile when the aspect ratio deviates from 1.0.

In the literature, various empirical formulations have been developed relating the coordination number and the void ratio. We can see that the coordination number decreases with the increase in the void ratio for a certain sandpile. Deng et al. [55] pointed out that a smaller CN does not necessarily mean higher porosity for ellipsoidal particles, or vice versa. Our results display the same behaviour. Compared with the other ellipsoids, the too-flat or too-elongated particles induce a higher coordination number with a higher void ratio.

4.1.3 Contact orientation

Different behaviour of void ratio and coordination number imply different arrangements of particles, which would induce various characteristics of contact networks with different particle aspect ratios. We examine the behaviour of the contact network in terms of contact vector, which refers to the vector from the contact point to the particle centre for the non-spherical particles. The orientation of contacts within an entire assembly can be characterized by the angular distribution $(E(\theta))$, which refers to the number of contacts falling within an angular interval $\Delta\theta$ [56]. In the three-dimensional space, the density is expressed by the portion of contacts per unit area on the unit sphere. Figure 9 portrays the 3D histogram of the contact orientation. Particles with an aspect ratio close to unity have a marked performance for the vertical contacts. When the aspect ratio deviates from 1.0, the initial structure
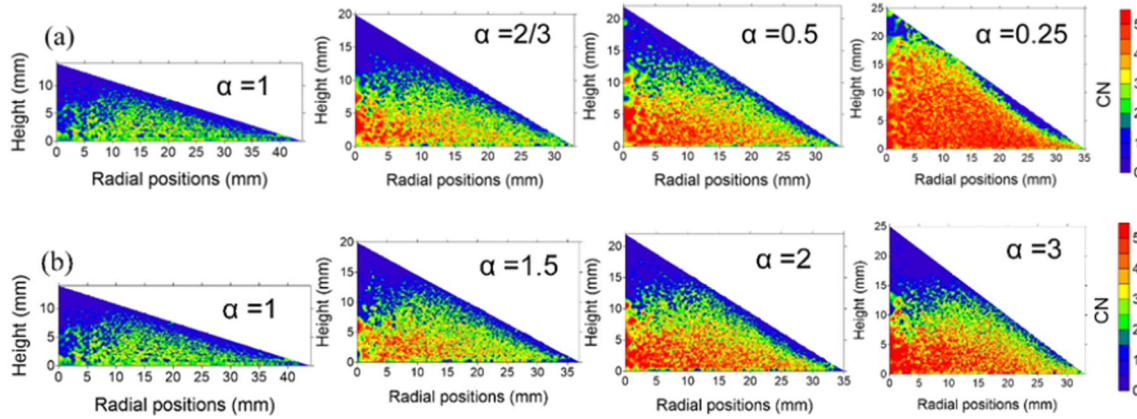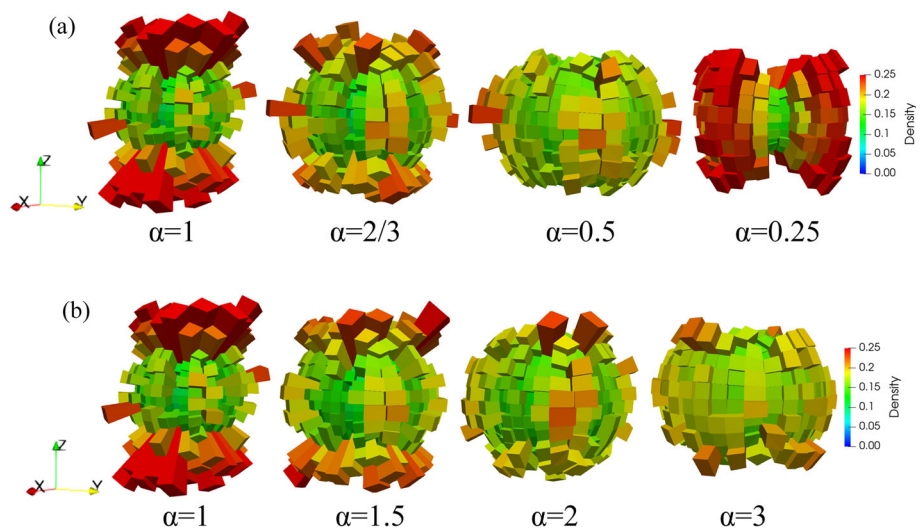
Fig. 8 Spatial distribution of CN: **a** oblate particles and **b** prolate particles

Fig. 9 Frequency of the contact orientation with different aspect ratios: **a** oblate particles and **b** prolate particles

shows a higher frequency of interparticle interaction in the horizontal plane and reduces the possibility of vertical interactions. The tilted contacts of the ellipsoidal particles would transfer the force to the outer edges of the sandpile and reduce the normal pressure.

4.2 Impact of construction histories

The induced heterogeneous geometry occurs due to the collapse of the initial granular structure subjected to the loading of particles. This subsection aims to observe the external loading of particles on the evolution of the mechanical behaviour in the inner region, which is defined in the cylindrical coordinate system by the radial position of 20 mm and the repose angle of 33°. In the following data analysis, the initial stage is denoted as the S1 stage. Two intermediate stages, the S2 stage and S3 stage, are determined by the increased deposited particles (ΔN_p), where ΔN_p is approximately 28,000. The number of particles for the S2 stage and S3 stage is approximately 45,000 and 73,000, respectively. The S4 stage refers to the final state of the simulation.

4.2.1 Evolution of void ratio

Figure 10 portrays the temporal probability distribution of the void ratio. In the inner region, the spherical particles produce a narrow distribution with a higher probability that occurs in the span of (0.5, 0.8). When particles become non-spherical, the local geometry has a higher possibility of a larger void ratio. Due to a smaller repose angle, the spherical particles would have better particle flowability. In such a case, particles near the spherical shape alter the void ratio significantly during the subsequent loading process. Moreover, the results indicate that the system is in a relatively stable condition when particles become too flat or elongated. The loading would only induce a slight change in the initial granular texture with a similar probability distribution of the void ratio during construction.

4.2.2 Evolution of coordination number

Figure 11 depicts the average coordination number of the inner region with different aspect ratios. At the initial stage, according to Fig. 8, the spherical particles produce a significantly lower average coordina-
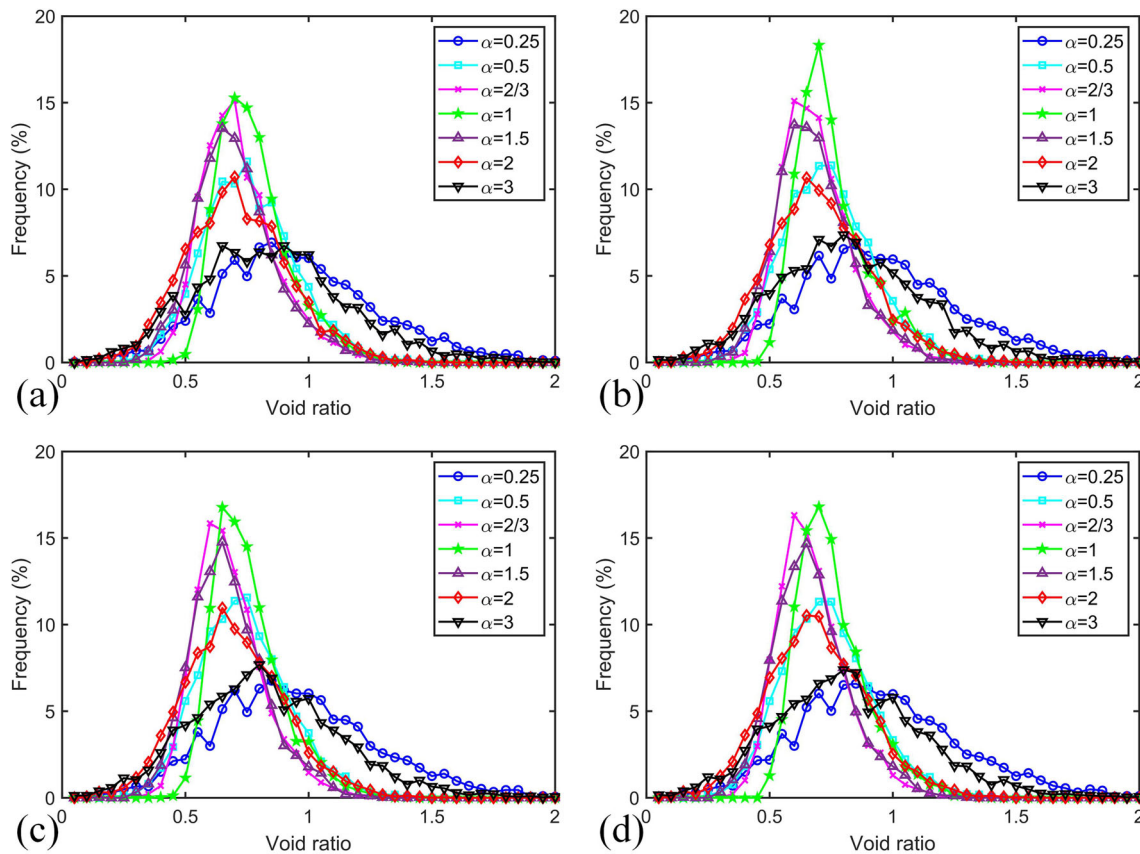
Fig. 10 Probability distribution of void ratio at: **a** S1 stage, **b** S2 stage, **c** S3 stage and **d** S4 stage

tion number, which enhances when the aspect ratio deviates from 1.0. The construction process alters the results of spherical particles significantly. Similar to the behaviour of void ratio, the external loading subjected to the deposition process causes tiny variations in the average coordination number for the too-flat/elongated particles. Compared with the elongated particles, the flat particles produce a more similar coordination number during construction. The results indicate that the too-flat particles contain a higher ability to maintain the initial structure.

4.2.3 Evolution of contact orientation

We convert the contact vector in the Cartesian coordinate system into the cylindrical coordinate system, using Eq. 11, for examining the characteristics of contact orientation (φ). Figure 12 illustrates the definition of the orientation of a contact vector in the cylindrical coordinate system. According to the graph, the angle of $90°$ refers to the z-axis. In the three-dimensional space, the orientation angle should be in a span of $(0 \sim 360°)$. However, concerning the axis-symmetrical condition, the spatial morphology of contact vectors with the angle of $(180 \sim 360°)$ should be the same as the results in the angle of $(0 \sim 180°)$. Hence, we are only concerned with the results varying from $0°$ to $180°$ to simplify the analysis. Figure 13 portrays the orientation frequencies of the contact vectors at temporal stages. The graph shows
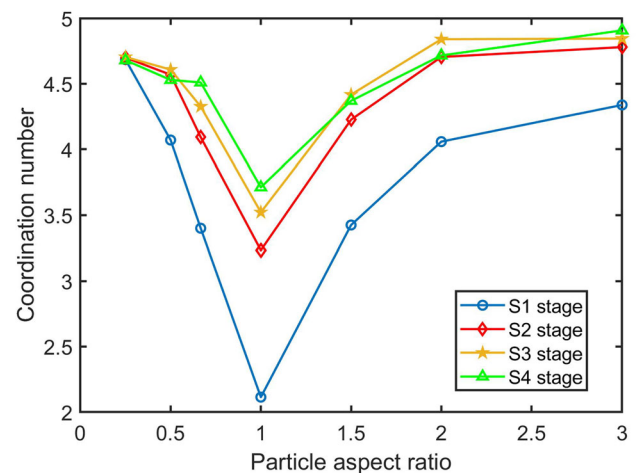

Fig. 11 Behaviour of average coordination number at different stages

spherical particles induce the peak frequency of contact orientation gradually rotated to the vertical interactions during construction. However, with the development of sandpiles, the ellipsoidal particles produce a similar probability distribution of the contact orientation, with the preference interactions tilted with the z-axis. The flat particle has a higher frequency for the contact orientation at approximately $45°$, which is at $135°$ for the elongated particles.

Fig. 12 Definition of the orientation of a contact vector
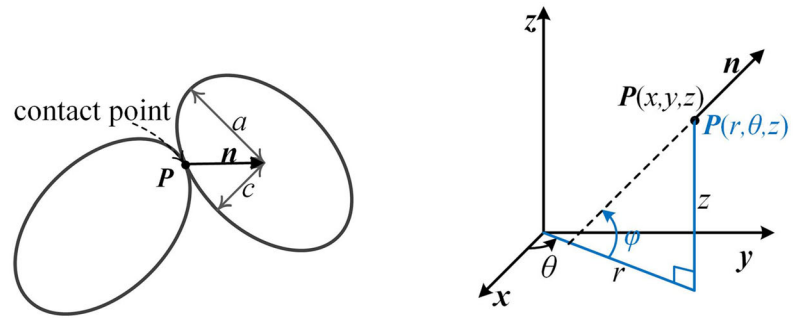
(a) Definition of two ellipsoids in contact   (b) Cartesian and cylindrical coordinate system for a contact vector
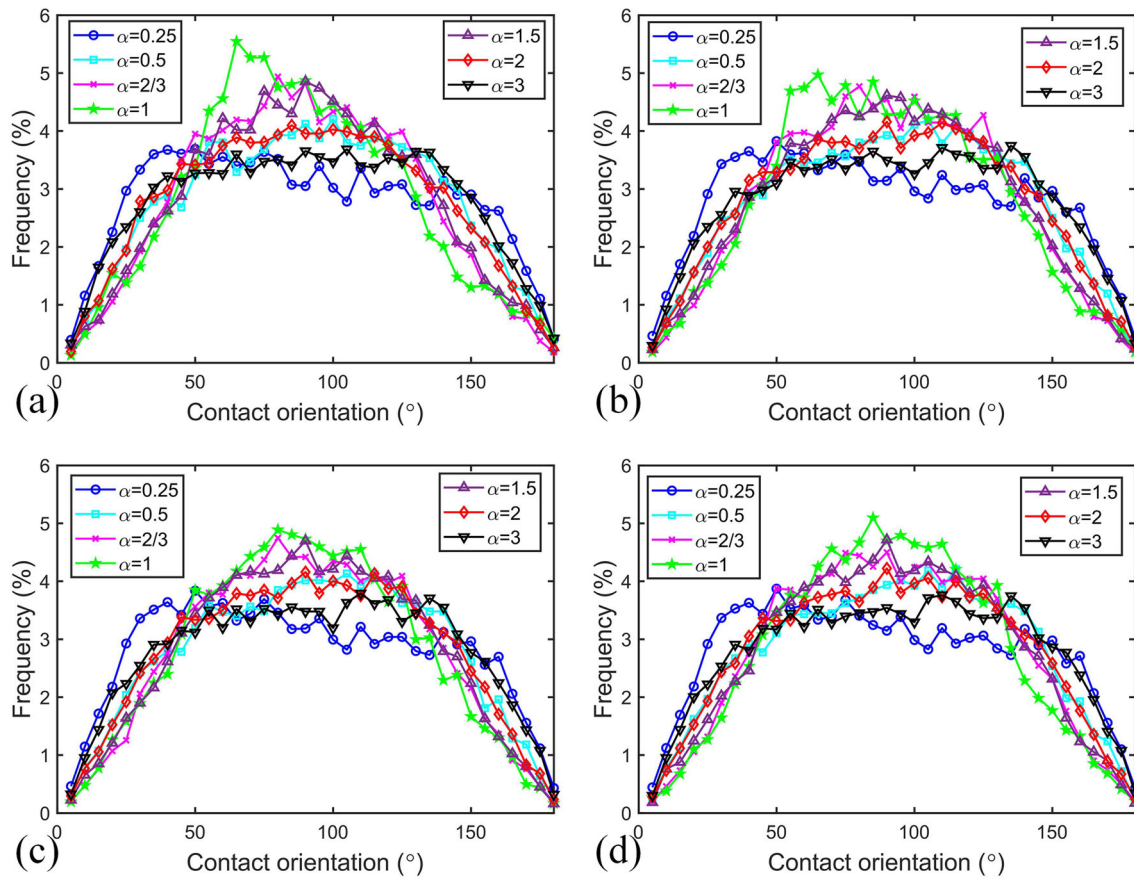

Fig. 13 Probability distribution of contact orientation at: **a** S1 stage, **b** S2 stage, **c** S3 stage and **d** S4 stage

5 Contact force

The internal structure only provides partial information about the interaction between the particles. The pressure profile highly depends on the granular texture and the force transmission. Hence, it requires considering the strength of the contacts to obtain a deeper understanding of the sandpile system.

5.1 Initial state

In analogy to the contact orientation, Fig. 14 depicts the 3D histogram of contact force at the initial state, where each bar represents a normalized local average

normal contact force in that orientation. Strong contact forces mainly form in the vertical direction due to the deposition method, particularly for the spherical particles. When the aspect ratio deviates from 1.0, the strong contact force rotates away from the z-axis. Ellipsoidal particles would thus transmit forces along the tilted direction to reduce the normal pressure underneath the apex.

5.2 Impact of construction histories

In the deposition process, the external loading can cause the creation, disruption and re-orientation of the contact network. Kruyt [57] pointed out that sepa-

Fig. 14 3D histogram of contact force: **a** oblate particles and **b** prolate particles

(a)

α =1   α =2/3   α =0.5   α =0.25
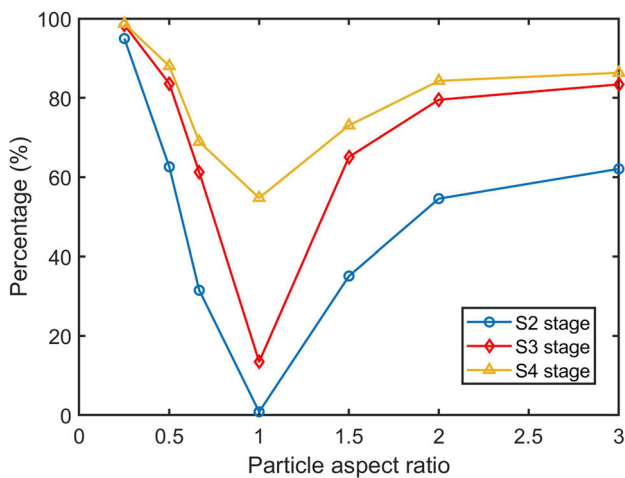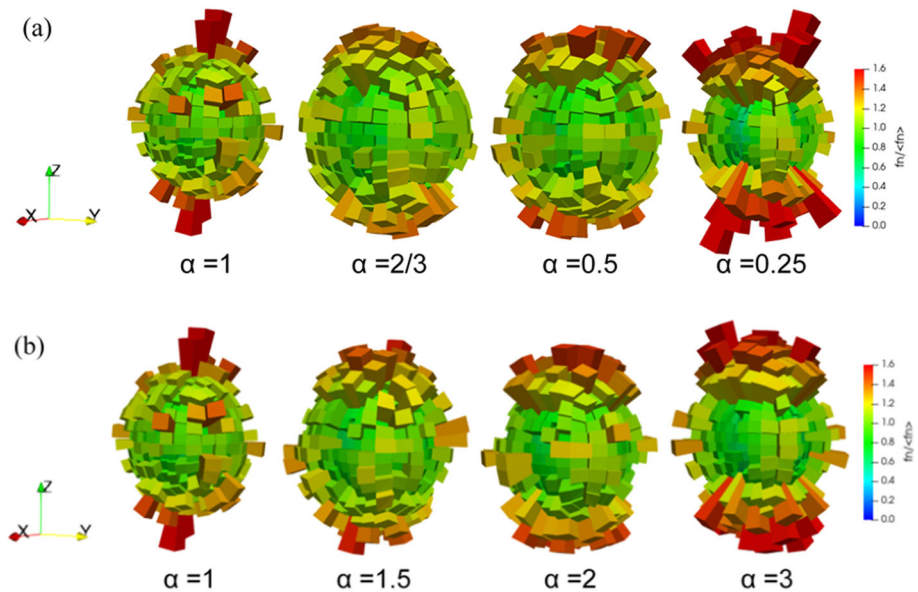
(b)

α =1   α =1.5   α =2   α =3

Fig. 15 Particle aspect ratio on the frequency of maintained contacts

rately studying the three mechanisms can bring insight into the structural changes to the contact network that occur during deformation.

When comparing two adjacent states, the local geometry of the current state can be expressed as the union of the maintained contacts and gained contacts. Figure 15 portrays the percentage of the maintained contacts at different temporal stages, which shows a significant loss of the local geometry for the spherical particles, particularly in the S2 stage. The ellipsoidal particles can enhance the interlocking effect and increase the possibility of maintaining the initial local geometry. The soil skeleton is almost the same during construction for the too-flat particles. As the number of particles grows, the structure becomes more stable. The results indicate that the ellipsoidal particles, particularly the too-flat particles, maintain the initial contacts longer than the spherical particles.

We examine the orientation of normal contact force to give a quantitative investigation of the mechanical roles of the contact subsets in force propagation. In analogy to the orientation of the contact vector defined in Fig. 12, the orientation of contact force is measured with respect to the r-axis. Figure 16 depicts the temporal behaviour of mean normal contact force at different aspect ratios. In the graphs, the solid lines refer to the results of the maintained contacts and the dashed lines are the behaviour of the gained contacts, where $< f_n >$ denotes the average normal contact force of the system. Radjai et al. [58] proposed that the contacts whose forces are larger than average forces are the strong forces. We can see that the strong forces are mainly supported by the maintained contacts when the aspect ratio deviates from 1.0, particularly for the too-flat particles. However, when the particles approach the spherical shape, the strong forces are carried by the maintained and gained interactions. The results indicate that the orientation of strong forces correlates to the particle shape, which produces a higher performance of strong contacts in the vertical direction under the subsequent loading of particles when the aspect ratio approaches 1.0. While the strong forces concentrate on a wider range during the formation process for the too-flat and too-elongated particles. Similar to the characteristics of internal structure, the ellipsoids, particularly the oblate particles, display a good memory of the behaviour of strong forces during construction.

The friction mobilization index (I_f) is adopted to examine the characteristics of tangential contact force (f_t), measured by $I_f = |ft|/\mu f_n$ at each contact. Due to the condition of the Coulomb friction law, the maximum value of I_f is 1.0, which corresponds to fully mobilized contacts. Figure 17 depicts the frequency of I_f in log-linear scales for different aspect ratios. The solid lines and dashed lines in the graphs also refer to the maintained contacts and gained contacts, respectively. The sandpile induces the primary peak probability at $I_f = 1.0$, while a secondary hump is observed
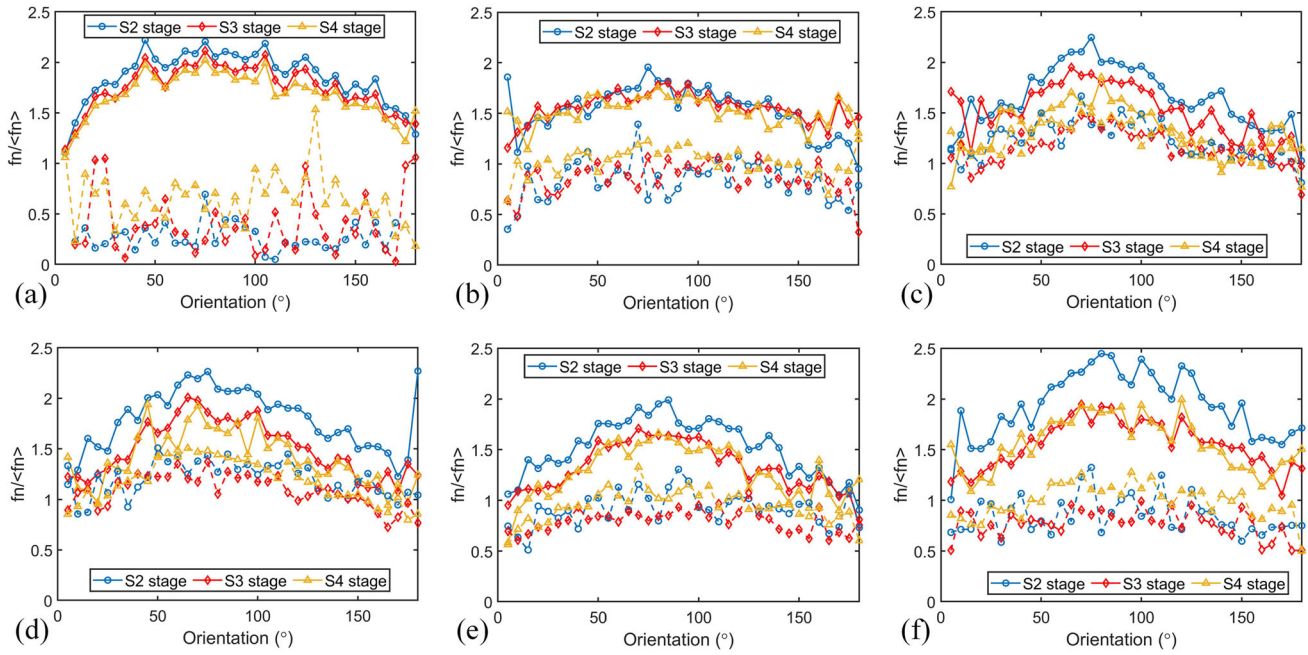
Fig. 16 Orientation of normal contact force for the aspect ratio of: **a** $\alpha = 0.25$, **b** $\alpha = 0.5$, **c** $\alpha = 2/3$, **d** $\alpha = 1.5$, **e** $\alpha = 2$ and **f** $\alpha = 3$

at $I_f \approx 0.3$ when the particles approach the spherical shape. The results suggest that the proportion of weakly mobilized contacts decreases and the proportion of highly mobilized contacts increases with the aspect ratio deviating from 1.0. The graphs display a similar probability distribution of I_f at different temporal stages for each aspect ratio. Moreover, the work of contact subsets only produces an obvious contrast for the too-flat particles.

6 Discussions

The temporal characteristics of internal structure and contact force indicate the ellipsoidal particles can have a better memory of the initial structure. The higher performance on maintaining the initial tilted strong contacts would transfer the stress to the outer edges to form the pressure dip phenomenon. We further examine the impact of contact subsets on the evolution of the stress state to elucidate the underlying mechanisms of the counter-intuitive phenomenon. The microstructural definition of the stress tensor is determined with the help of the individual contact forces inside the assembly of grains, which could be expressed in terms of discrete micro variables as,

$$\sigma_{ij} = \frac{1}{V} \sum f_i l_j \qquad (12)$$

where σ_{ij} is the average stress tensor, V is the volume of Voronoi cells, f_i is the component of the contact force in the ith direction, and l_j is the contact vector.

According to the definition of the stress tensor, the stress state can be subdivided into two parts concerning the maintained and gained contacts, expressed as,

$$\sigma_{ij} = \sigma_{ij}^M + \sigma_{ij}^G = \frac{1}{V} \sum f_i l_j^M + \frac{1}{V} \sum f_i l_j^G \qquad (13)$$

where σ_{ij}^M and σ_{ij}^G are the stress tensor of the maintained contacts and gained contacts, respectively. l_j^M and l_j^G denote the contact vector of maintained contacts and gained contacts, respectively.

The stress state is also analysed in the cylindrical coordinate system concerning the axis-symmetrical conical sandpile. Adopting Eq. 13, we first estimate the stress tensor (σ_{ij}) of each particle in the Cartesian coordinate system and then transfer the results to the cylindrical coordinate system using the following equation,

$$\left[\sigma_{ij}^r \right] = \left[Q^{\mathrm{T}} \right] \left[\sigma_{ij} \right] \left[Q \right] \qquad (14)$$

in which Q is the transformation matrix and equals to $\begin{bmatrix} \cos\theta & -\sin\theta & 0 \\ \sin\theta & \cos\theta & 0 \\ 0 & 0 & 1 \end{bmatrix}$. θ is the location of particle in the cylindrical coordinate system and σ_{ij}^r is the stress tensor in the cylindrical coordinate system.

Figure 18 gives the evolution of stress components for σ_{ij}^M and σ_{ij}^G with different aspect ratios. Depending on the conical shape, the stress tensor should be axis-symmetrical along the θ plane in the cylindrical coordinate system, which implies the stress tensor $\sigma_{r\theta}$ and $\sigma_{\theta z}$ are around zero and thus do not display. σ_{rr} produces a similar behaviour as $\sigma_{\theta\theta}$. Due to the self-gravity impact, the sandpiles produce major stress in the vertical direction and enhance with the development of
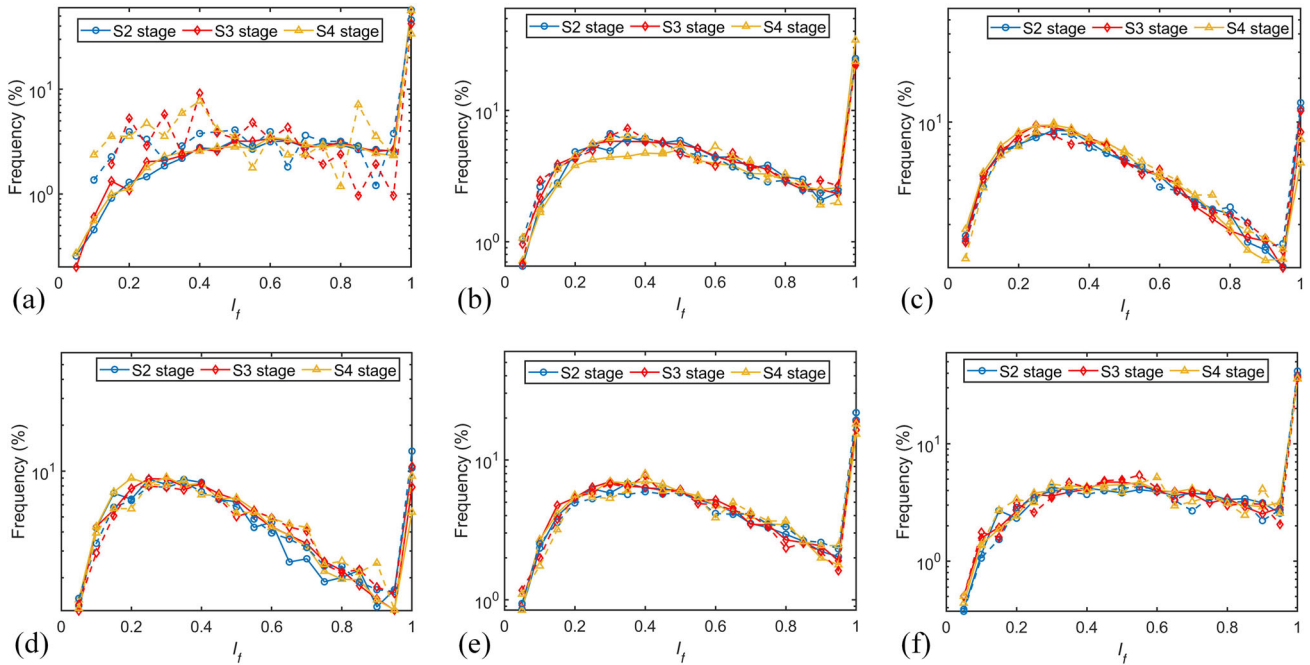
Fig. 17 Orientation of I_f for the aspect ratio of: **a** $\alpha = 0.25$, **b** $\alpha = 0.5$, **c** $\alpha=2/3$, **d** $\alpha=1.5$, **e** $\alpha=2$ and **f** $\alpha=3$
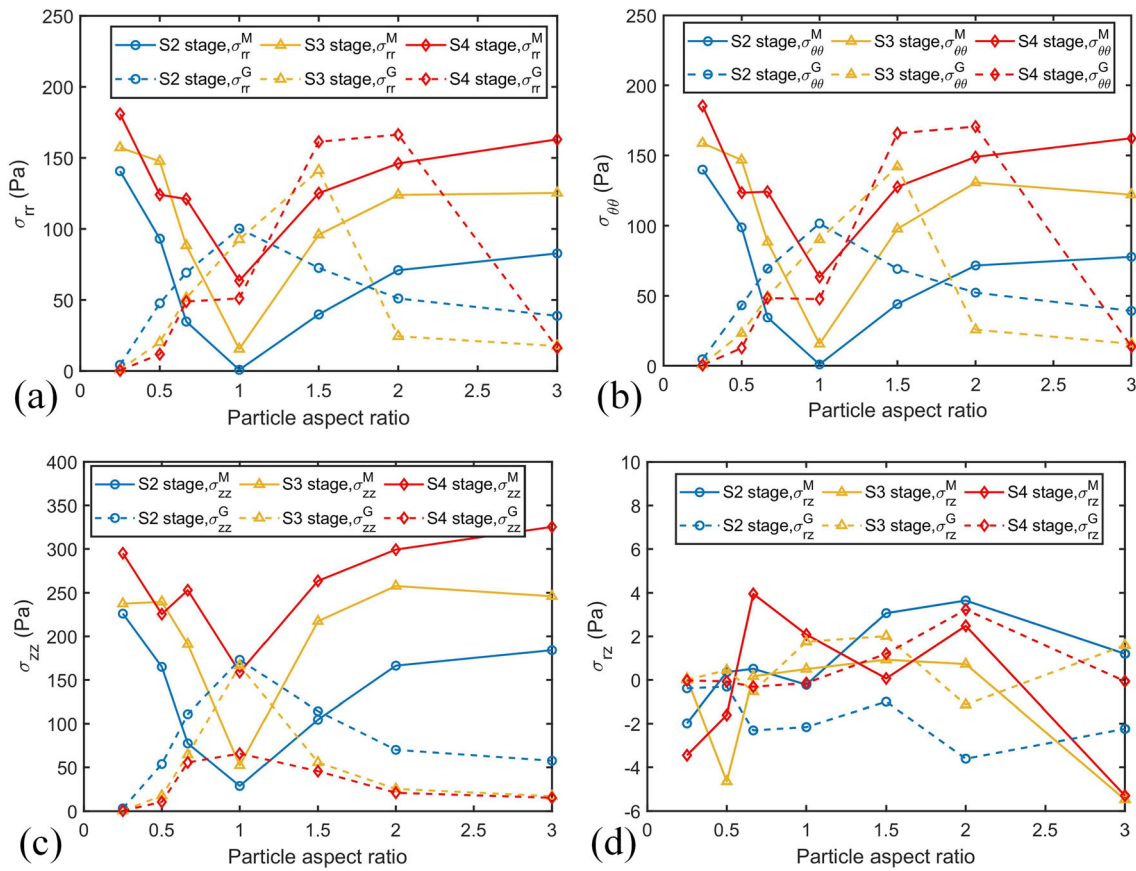

Fig. 18 Evolution of the stress components with different aspect ratios: **a** σ_{rr}, **b** $\sigma_{\theta\theta}$, **c** σ_{zz} and **d** σ_{rz}

sandpiles. Compared with the stress components in the diagonal direction, σ_{rz} is significantly lower and close to zero. According to Fig. 9, the initial tilted contact vectors of the too-flat and too-elongated particles produce a higher stress field in the (r, θ) space, which propagates the stress in a diffusive condition.

At each temporal stage, when the aspect ratio deviates from 1.0, the maintained contacts display an increase in σ_{rr}^M, $\sigma_{\theta\theta}^M$ and σ_{zz}^M, while the gained contacts have the reverse effect. We can see that the deposited spherical particles induce zero horizontal stress at the initial stage, while the newly created interactions enhance the fraction of horizontal stress during construction. For particles with $\alpha = 2$, it is interesting to observe that the newly generated interactions induce a major stress in the horizontal plane, which thus produces a remarked pressure dip phenomenon than the other ellipsoids. The results indicate that the gained contacts of prolate particles play a more vital role in stress propagation than the oblate particles. Similar to the behaviour of contact force, the stress state of the too-flat particles is primarily contributed by σ_{ij}^M, which agrees with the assumption proposed by Wittmer et al. [47]. However, when the aspect ratio approaches 1.0, the stress state behaves as a joint result of maintained and gained contacts. Hence, additional and complex models have to be formulated concerning contact creation to capture the pressure profile when contacts are not fairly permanent.

7 Conclusions

In this paper, we consider three-dimensional simulations of sandpile systems built from different shapes of ellipsoids and study the structural properties and contact force on the characteristics of stress propagations. The ellipsoidal particles can produce a denser sandpile and significant pressure dip phenomenon within a specific range of aspect ratios. However, the too-flat or elongated particles would enhance the void ratio inside the sandpile. We examined the impact of particle shape on the memory of the initial structure via the underlying mechanisms of initial granular structure and induced heterogeneous geometry. For the initial stage, particles with different aspect ratios induce different local internal structures and contact forces. The contact vector and strong contact force rotate away from the z-axis when the aspect ratio deviates from 1.0. Concerning the construction process, the ellipsoidal particles enhanced the interlocking effect. In the inner region, the too-flat particles have a better memory of the initial structure, with the strong contact force carried by the maintained contacts. However, when the particle is close to a spherical shape, the stress state behaves as a joint result of maintained and gained contacts. For a specific range of aspect ratios, the newly generated interactions of elongated particles induced the major principal stress in the horizontal plane, which thus produces a significant pressure dip phenomenon. Our study sheds some insight into the underlying mechanisms of sandpiles.

granular packings. However, we only examine the mono-sized non-spherical particles. Studying the polydispersity of the non-spherical particles can further understand the memory of initial structure on the behaviour of granular materials and advance the understanding in process engineering like additive manufacturing and biomass combustion.

References

1. P. Richard, M. Nicodemi, R. Delannay, P. Ribiere, D. Bideau, Slow relaxation and compaction of granular system. Nat. Mater. **4**(2), 121–128 (2005)
2. X. Gao, J. Yu, J.F. Ricardo, J.F. Dietike, M. Shahnam, W.A. Rogers, Development and validation of Super-DEM for non-spherical particulate systems using a superquadric particle method. Particuology **61**, 74–90 (2021)
3. Y. Fan, Y. Boukerkour, T. Blanc, P.B. Umbanhowar, J.M. Ottino, R.M. Lueptow, Stratification, segregation, and mixing of granular materials in quasi-two-dimensional bounded heaps. Phys. Rev. E **86**, 051305 (2012)
4. H.A. Makse, S. Havlin, P.R. King, H.E. Stanley, Spontaneous stratification in granular mixtures. Nature **386**, 379–382 (1997)
5. F.H. Hummel, E.J. Finnan, The distribution of pressure on surfaces supporting a mass of granular material. Proc. Inst. Civ. Eng. **212**, 369–392 (1920)
6. B. Brockbank, J. Huntley, R. Ball, Contact force distribution beneath a three-dimensional granular pile. J. Phys. II EDP Sci. **7**(10), 1521–1532 (1997)
7. H.-G. Matuttis, Simulation of the pressure dip phenomenon under a two-dimensional heap of polygonal particles. Granul. Matter **1**, 83–91 (1998)
8. I. Zuriguel, T. Mullin, J.M. Rotter, Effect of particle shape on the stress dip under a sandpile. Phys. Rev. Lett. **98**(2), 028001–028004 (2007)
9. I. Zuriguel, T. Mullin, The role of particle shape on the stress distribution in a sandpile. Proc. R. Soc. A Math. Phys. Eng. Sci. **464**(2089), 99–116 (2008)
10. C. Zhou, J. Ooi, Numerical investigation of progressive development of granular pile with spherical and non-spherical particles. Mech. Mater. **41**(6), 707–714 (2009)
11. J.Y. Zhu, Y.Y. Liang, Y.H. Zhou, The effect of the particle aspect ratio on the pressure at the bottom of sandpiles. Powder Technol. **234**, 37–45 (2013)
12. Z.Y. Zhou, R.P. Zou, D. Pinson, A.B. Yu, Angle of repose and stress distributions of sandpiles formed with ellipsoidal particles. Granul. Matter **16**, 695–709 (2014)
13. Y.Y. Liu, A.T. Yeung, D.L. Zhang, Y.R. Li, Experimental study on the effect of particle shape on stress dip in granular sandpiles. Powder Technol. **319**, 415–425 (2017)

14. J.G. Liu, Q.C. Sun, F. Jin, The influence of flow rate on the decrease of pressure beneath a conical sandpile. Powder Technol. **212**, 296–298 (2011)

15. J. Ai, J.Y. Ooi, J. Chen, J.M. Rotter, Z. Zhong, The role of deposition process on pressure dip formation underneath a granular pile. Mech. Mater. **66**, 160–171 (2013)

16. J. Ai, Particle scale and bulk scale investigation of granular piles and silos. Ph.D. thesis, University of Edinburgh (2010)

17. Y.C. Zhou, B.H. Xu, R.P. Zou, A.B. Yu, P. Zulli, Stress distribution in a sandpile formed on a deflected base. Adv. Powder Technol. **14**, 401–410 (2003)

18. J.Y. Ooi, J. Ai, Z. Zhong, J.F. Chen, J.M. Rotter, *Progressive pressure measurements beneath a granular pile with and without base deflection. Structures and granular solids: from scientific principles to engineering applications* (CRC Press, London, 2008), pp.87–92

19. B.W. Fitzgerald, A. Zarghami, V.V. Mahajan, S.K. Sanjeevi, I. Mema, V. Verma, J.T. Padding, Multiscale simulation of elongated particles in fluidised beds. Chem. Eng. Sci. X **2**, 100019 (2019)

20. H.G. Matuttis, S. Luding, H.J. Herrmann, Discrete element simulations of dense packings and heaps made of spherical and non-spherical particles. Powder Technol. **109**(1), 278–292 (2000)

21. C. Zhou, J. Ooi, Numerical investigation of progressive development of granular pile with spherical and non-spherical particles. Mech. Mater. **41**(6), 707–714 (2009)

22. J. Ai, J.F. Chen, J.M. Rotter, J.Y. Ooi, Numerical and experimental studies of the base pressures beneath stockpiles. Granul. Matter **13**(2), 133–141 (2011)

23. J.Y. Zhu, Y.Y. Liang, Y.H. Zhou, The effect of the particle aspect ratio on the pressure at the bottom of sandpiles. Powder Technol. **234**, 37–45 (2013)

24. Y.Y. Liu, A.T. Yeung, D.L. Zhang, Y.R. Li, Experimental study on the effect of particle shape on stress dip in granular sandpiles. Powder Technol. **319**, 415–425 (2017)

25. N. Topic, J.A.C. Gallas, T. Pöschel, Characteristics of large three-dimensional heaps of particles produced by ballistic deposition from extended source. Philos. Mag. **93**(31–33), 4090–4107 (2013)

26. J.M. Ting, M. Khwaja, L.R. Meachum, J.D. Rowell, An ellipse-based discrete element model for granular materials. Int. J. Numer. Anal. Methods Geomech. **17**, 603–623 (1993)

27. R.B.S. Oakeshott, S.F. Edvards, Pertubative theory of the packing of mixtures and non-spherical particles. Phys. A **202**, 482–498 (1994)

28. C. Hogue, D. Newland, Efficient computer computation of moving granular particles. Powder Technol. **78**, 51–66 (1994)

29. M.A. Hopkins, Numerical Simulation of Systems of Multitudinous Polygonal Blocks. USARREL Report CR 99-22, US Army Cold Regions Research and Engineering Laboratory (1992)

30. J.A.C. Gallas, S. Sokolowski, Grain non-sphericity effects on the angle of repose of granular material. Int. J. Mod. Phys. B **7**(9 & 10), 2037–2046 (1993)

31. B. Soltanbeigi, A. Podlozhnyuk, S.A. Papanicolopulos, C. Kloss, S. Pirker, J.Y. Ooi, DEM study of mechanical characteristics of multi-spherical and superquadric particles at micro and macro scales. Powder Technol. **329**, 288–303 (2018)

32. A.H. Barr, Superquadrics and angle-preserving transformations. IEEE Comput. Graph. Appl. **1**(January), 11–23 (1981)

33. J.R. Williams, A.P. Pentland, Superquadratics and modal dynamics for discrete elements in interactive design. Eng. Comput. **9**, 115–127 (1992)

34. C. Ericson, *Real-Time Collision Detection* (CRC Press, New York, 2005)

35. A. Podlozhnyuk, S. Pirker, C. Kloss, Efficient implementation of superquadric particles in discrete element method within an open-source framework. Comput. Part. Mech. **4**(1), 101–118 (2016)

36. Y. Tsuji, T. Tanaka, T. Ishida, Lagrangian numerical simulation of plug flow of cohesionless particles in a horizontal pipe. Powder Technol. **71**, 239–250 (1992)

37. N. Martys, R.D. Mountain, Velocity Verlet algorithm for dissipative-particle-dynamics-based models for suspensions. Phys. Rev. E **59**, 3733–3736 (1999)

38. P.W. Cleary, M.L. Sawley, DEM modelling of industrial granular flows: 3D case studies and the effect of particle shape on hopper discharge. Appl. Math. Model. **26**(2), 89–111 (2002)

39. L. Vanel, D. Howell, D. Clark, R.P. Behringer, E. Clement, Memories in sand: Experimental tests of construction history on stress distributions under sandpiles. Phys. Rev. E **60**(5), 5040–5043 (1999)

40. K.L. Johnson, *Contact Mechanics* (Cambrige University Press, Cambrige, 1985)

41. W.C. Li, G. Deng, Q. Zhang, Q. Zhong, X. Sun, L. Lee, Comparison of continuum stresses in granular material computed by volume average approach and boundary average approach under static and quasi-static conditions. Int. J. Appl. Mech. **13**(08), 2150095 (2021)

42. J.F. Geng, E. Longhi, R.P. Behringer, D.W. Howell, Memory in two dimensional heap experiments. Phys. Rev. E **64**(6), 060301–060304 (2001)

43. A.V. Kyrylyuk, A.P. Philipse, Effect of particle shape on the random packing density of amorphous solids. Phys. Status Solidi A **208**(10), 2299–2302 (2011)

44. Z. Zhou, R. Zou, D. Pinson, A. Yu, Discrete modelling of the packing of ellipsoidal particles. AIP Conf. Proc. **1542**, 357 (2013)

45. H.M.B. Al-Hashemi, O.S.B. Al-Amoudi, A review on the angle of repose of granular materials. Powder Technol. **330**, 397–417 (2018)

46. A. Mehta, G.C. Barker, The dynamics of sand, reports. Prog. Phys. **57**, 383–416 (1994)

47. J.P. Wittmer, P. Claudin, M.E. Cates, J.P. Bouchaud, An explanation for the central stress minimum in sand piles. Nature **382**(25), 336–338 (1996)

48. J.P. Wittmer, M.E. Cates, P. Claudin, Stress propagation and arching in static sandpiles. J. Phys. I EDP Sci. **7**(1), 39–80 (1997)

49. V.A. Luchnikov, N.N. Medvedev, L. Oger, J.-P. Troadec, Voronoi-Delaunay analysis of voids in systems of nonspherical particles. Phys. Rev. E **59**, 7205 (1999)

50. R. Al-Raoush, K.A. Alshibli, Distribution of local void ratio in porous media systems from 3D X-ray microtomography images. Phys. A Stat. Mech. Appl. **361**, 441–456 (2006)

51. F.M. Schaller, S.C. Kapfer, M.E. Evans, M.J.F. Hoffmann, T. Aste, G.E. Schroder-Turk, Set Voronoi diagrams of 3D assemblies of aspherical particles. Philos. Mag. **93**(31–33), 3993–4017 (2013)
52. A. Baule, H.A. Makse, Fundamental challenges in packing problems: from spherical to non-spherical particle. Soft Matter **10**, 4423–4429 (2014)
53. H.A. Makse, D.L. Johnson, L.M. Schwartz, Packing of compressible granular materials. Phys. Rev. Lett. **84**, 4160–4163 (2000)
54. J. Horabik, P. Parafiniuk, M. Molenda, Discrete element modelling study of force distribution in a 3D pile of spherical particles. Powder Technol. **312**, 194–203 (2017)
55. X. Deng, J. Scicolone, R.N. Dave, Discrete element method simulation of cohesive particles mixing under magnetically assisted impaction. Powder Technol. **243**, 96–109 (2013)
56. S. Zhao, X. Zhou, Effects of particle asphericity on the macro and micro-mechanical behaviours of granular assemblies. Granul. Matter **19**(2), 3 (2017)
57. N.P. Kruyt, Micromechanical study of fabric evolution in quasi-static deformation of granular materials. Mech. Mater. **44**, 120–129 (2012)
58. F. Radjai, S. Roux, J.J. Moreau, Contact forces in a granular packing. Chaos **9**, 544 (1999)